Manuel, M., Sedky, G., Jones, A.R., Flores, O., García-Villalba, M. (2021). Characterization of Aerodynamic Forces on Wings in Plunge Maneuvers. *AIAA Journal*, 59(2), 736-747.

DOI: https://doi.org/10.2514/1.J059689

Characterization of aerodynamic forces on wings in plunge maneuvers

Manuel Moriche,*
Karlsruhe Institute of Technology, 76131 Karlsruhe, Germany

Girguis Sedky†, Anya R. Jones‡
University of Maryland, College Park, MD, 20742, USA

Oscar Flores§, Manuel García-Villalba¶
Carlos III University of Madrid, 28911 Leganés, Spain

We present experiments and simulations of plunging maneuvers of large amplitude, for velocity ratios $G = 1$ and 2, defined as the ratio between the peak plunge velocity and the freestream velocity. We explore the effect of the airfoil shape by considering a NACA0012 wing and a flat plate. The experiments are performed with wings of aspect ratio 4 and 4.86, while the simulations are performed using a model of an infinite aspect-ratio wing. We report the time evolution of the force coefficients and flow visualizations. A good qualitative agreement is found between experiments and simulations, with small discrepancies in the maximum and minimum lift coefficients observed during the maneuvers, and somewhat larger discrepancies during the post-maneuver phase. It is found that the airfoil shape has a small effect on the lift coefficient but a somewhat larger effect on the drag coefficient. We also perform a force decomposition analysis to relate vortical structures to the force on the wings providing a quantitative measurement of the effect of leading edge vortex and trailing edge vortex on the peak aerodynamic forces.

Nomenclature

AR	Aspect ratio of the wing
c	Chord length
C_D	Drag coefficient

*Postdoctoral Researcher, Institute for Hydromechanics. Kaiserstr. 12.
†Graduate Research Assistant, Department of Aerospace Engineering, AIAA Student Member. 3179 Glenn L. Martin Hall.
‡Associate Professor, Department of Aerospace Engineering, AIAA Associate Fellow. 3179 Glenn L. Martin Hall.
§Associate Professor, Department of Bioengineering and Aerospace Engineering. Avenida de la Universidad 30.
¶Associate Professor, Department of Bioengineering and Aerospace Engineering, AIAA Senior Member. Avenida de la Universidad 30.
Partial results presented in conference paper "Comparison between experiments and simulations of fast tranverse plunge maneuvers", 5-1-2020, AIAA Scitech 2020 Forum.

C_L	Lift coefficient
$C_L^{\max}$	Maximum of the lift coefficient
$C_L^{\min}$	Minimum of the lift coefficient
C_N	Normal force coefficient
D	Drag force
$\vec{e}_x$	Unit vector along x direction
$\vec{e}_z$	Unit vector along z direction
G	Velocity ratio $G = V_{\max}/U_\infty$
h	Maneuver height
L	Lift force
$\vec{n}$	Unit vector normal to the airfoil
Re	Reynolds number $Re = U_\infty c/\nu$
S	Wing surface
T	Maneuver duration
$\vec{u}$	Relative velocity of the fluid with respect to the wing
$\vec{u}_w$	Wing velocity with respect to a reference frame which is at rest
u_y^{std}	Standard deviation of the spanwise velocity with respect to the spanwise average
U_∞	Free stream velocity
V	Fluid domain
$V_{\max}$	Maximum vertical velocity of maneuver
w	Maneuver width
α	Geometric angle of attack of the wing
δ_D	Drag density
δ_L	Lift density
ν	Kinematic viscosity of the fluid

μ	Dynamic viscosity of the fluid
ρ	Density of the fluid
$\vec{\omega}$	Vorticity
$\overline{\omega}_y$	Spanwise vorticity averaged along the spanwise direction
ϕ_x	Projection function along x direction
ϕ_z	Projection function along z direction

I. Introduction

There is a growing interest in characterizing force production on wings in unsteady situations. As fixed and flapping wing micro air vehicles are made smaller, modeling their aerodynamic response in a uniform free stream becomes unrealistic. Ambient air is never steady, and as the vehicle becomes smaller the perturbations in the surrounding air become comparable with the size and velocity of the vehicle, producing large fluctuations in the aerodynamic forces [1] that challenge the stability and controllability of the vehicle [2]. Moreover, when the flow perturbations are of the same order of magnitude as the flight speed, classical solutions based on small perturbations and linear theory [3] are no longer applicable. The flow surrounding the wing is subject to non-linear phenomena involving flow separation and the formation of leading edge vortices (LEVs) and trailing edge vortices (TEVs) that substantially influence the aerodynamic forces on the wings. As a consequence, in order to predict the aerodynamic forces in such unsteady situations it is necessary to resort to experiments and time-dependent numerical simulations.

The flow perturbations in unsteady environments are highly variable, so researchers often consider canonical configurations to characterize the different contributions to the aerodynamic response of the wing. One recent example of the use of canonical configurations is the work of Leung et al. [4] who modelled transverse gusts using different airfoil motions: pitching, plunging and surging. Another example is the work of Mulleners et al. [5] as well as Granlund et al. [6] who modelled a streamwise gust using surging motions of the wing. Granlund et al. [6] investigated the utility of studying streamwise gusts using moving models by comparing experiments in a sinusoidally varying freestream with experiments with a sinusoidally moving airfoil. They arrived at a good agreement in the measured circulatory contribution of the force between the two experimental campaigns. In this study we focus on plunge maneuvers, but the literature on canonical motions is broad, including also pitch maneuvers [7–9], surging maneuvers [10] and wing rotation[11, 12]. There are limiting factors to simulating a transverse gust with a plunging motion. Potential flow analysis shows an additional buoyancy force experienced by the test model when the freestream is accelerated compared

to when the freestream is steady and the test model is accelerated [6]. In addition, using a plunging motion to capture the unsteady flow of a transverse gust fails to capture the non-uniform chord-wise velocity distribution encountered in a gust. Sedky et al. [13] showed that the effective angles of attack from the two scenarios are different, which may lead to different circulatory force contributions. Nevertheless, understanding the physical sources of the difference between the two scenarios is important, and may provide a way to correct for that difference when researchers interested in studying gust encounters do not have adequate experimental facilities to introduce a gust by oscillating the flow. For instance, understanding the source of discrepancy in the non-circulatory forces experienced by the wing between an oscillating approach stream and a moving test model helps to correct the added-mass component of the force in a gust study if a moving test model approach is taken. Granlund et al. [6] were able to reconcile the difference in the non-circulatory force between experiments with an oscillating stream and an oscillating test model by subtracting out the extra buoyancy force experienced during the sinusoidal oscillation of the freestream. The utility of plunging maneuvers is not limited to modeling transverse gusts, but also they have been used for their relation to flapping flight. For example, Wang [14] used a plunge maneuver to characterize the formation and detachment of the leading edge vortex; this led to the determination of the optimal frequency for the flapping motion.

More closely related to the modelling of gusts, Perrotta and Jones [15] performed unsteady force measurements on a plunging flat plate using a water-filled towing tank. The maneuvers were modeled after a sine-squared gust profile, to match the approximation of gust encounters and to facilitate comparison to gust encounter force measurements from previous experimental campaigns [16]. Forces were measured for a large variety of plunge maneuvers, varying the width and height traveled by the wing during the maneuver as well the geometric angle of attack of the wing. Moriche et al. [17] performed direct numerical simulations (DNS) using some of the kinematics of Perrotta and Jones[15], but for a model of an infinite aspect-ratio NACA0012 wing. The lift coefficient predicted in the simulations was found to be in qualitative agreement with the measurements, however, some quantitative discrepancies were observed. The reason behind these discrepancies was unclear, however, there were some obvious differences between experimental and computational setups, e.g. in the experiment a flat plate was studied while in the simulation a NACA0012 airfoil was considered. In order to reduce these differences, new force measurements and additional direct numerical simulations have been performed.

In this work, we report the comparison between the corresponding experiments and simulations, with the aim of characterizing the aerodynamic forces on the wings during the plunge maneuvers. The analysis is based on force measurements from the experimental campaign and on flow visualizations from the numerical simulations. We also employ a technique [18, 19] to decompose the aerodynamic force into several contributions with the aim of relating the flow structures to the force on the wing. The paper is organized as follows: in section II we introduce first the flow configuration under study, then we discuss the experimental setup and finally the computational setup. Results

are presented in section III. We present first the force coefficients for both experimental measurements and numerical results. This is followed by flow visualizations using vorticity contours and a measure of the three-dimensionality of the flow. Finally we report the analysis based on the force decomposition technique. Some conclusions are provided in section IV.

II. Methods

A. Flow configuration

The maneuvers considered in this study were defined by Perrotta and Jones [15] and modeled after a sine-squared gust profile. The motivation behind the selection of this profile was to match the canonical approximation of gust encounters [20] and to be able to compare to their previous transverse gust measurements [16]. The plunge maneuver is performed on a wing of chord c which is subject to a free stream of constant speed U_∞ and at time $t = 0$ is subject to a vertical motion with velocity

$$V(t) = -V_{\max} \sin^2\left(\frac{\pi t}{T}\right) \quad \text{for } 0 \le t \le T, \tag{1}$$

where $V_{\max}$ is the peak plunge velocity and T is the maneuver duration. Thus, the plunge maneuver consists of two phases, the acceleration phase until the maximum plunge velocity is reached and a subsequent deceleration phase until the vertical motion is stopped. The horizontal distance covered during the maneuver (or maneuver width) is given by $w = U_\infty T$ and the vertical distance (or maneuver height) is obtained by integration of (1), $h = V_{\max} T/2$. The velocity ratio is defined by $G = V_{\max}/U_\infty$, which is the ratio between the peak plunge velocity and the freestream velocity.

Perrotta and Jones [15] performed an extensive parametric study by varying velocity ratio, G, duration of the maneuver, T, and angle of attack of the wing, α. In the present study, due to the high computational cost of the direct numerical simulations, we focus on a small set of parameters driven by the previous study of Moriche et al. [17]. We fix the duration of the maneuver $T = 2c/U_\infty$ so that the width is also fixed, $w/c = 2$, and the height depends on the velocity ratio, $h/c = G$. We consider two velocity ratios, $G = 1$ and $G = 2$. Concerning the angle of attack of the wing, the results of Perrotta and Jones [15] show that for large G, as the ones considered here, and for small angle of attack, the resulting lift coefficient is not significantly affected by the particular value of the angle of attack. In preliminary direct numerical simulations it was observed that it was easier to trigger the three-dimensionality of the flow at $\alpha = 5^\circ$ than at $\alpha = 0^\circ$. Note also that for a symmetric airfoil there is no lift in steady conditions at $\alpha = 0^\circ$ so that $\alpha = 5^\circ$ might be a more relevant flight condition. As a consequence, we decided to perform the study fixing $\alpha = 5^\circ$. Finally, in order to evaluate the effect of the airfoil shape we consider two different shapes, a flat plate and a NACA0012 airfoil.

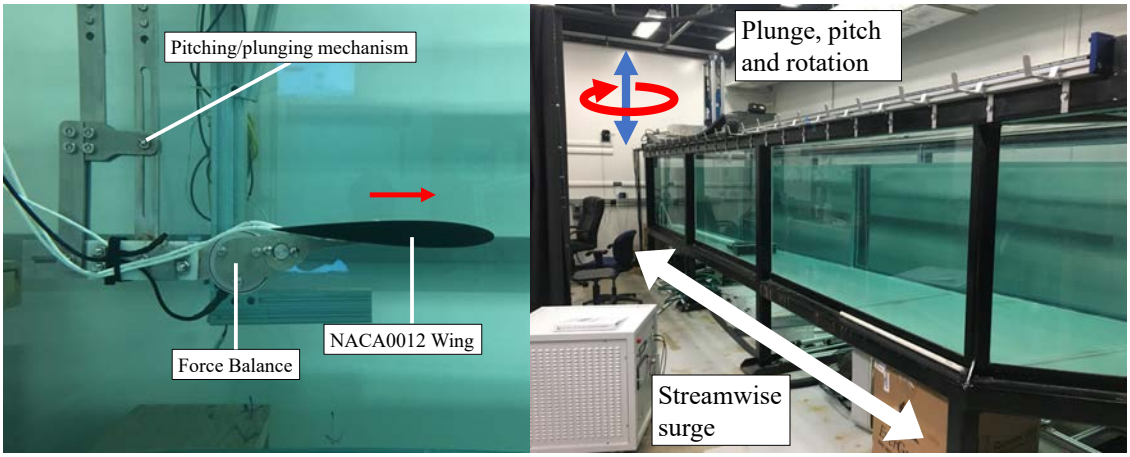

Fig. 1 Free-surface water towing tank facility and wing test setup

B. Experimental setup

Experimental data collection was conducted in a free-surface water towing tank at the University of Maryland. Figure 1 shows the water tank, which is 7m in length, 1.5 m in width, and 1 m in depth, as well as the wing test setup including the force balance and the pitching/plunging mechanism. The specifications of the facility can be found in Sedky et al. [13]. Plunging experiments were carried out at a Reynolds number $Re = 20,000$ to maintain an adequate signal-to-noise ratio in the force measurements. Three finite aspect ratio wings were studied: a NACA0012 wing with an aspect ratio $AR = 4.86$ and a chord length $c = 11.5$ cm, a NACA0012 wing with $AR = 4$ and a chord length $c = 7.62$ cm, and a flat plate with $AR = 4$, a chord length of $c = 7.62$ cm and 0.33 cm thickness. Table 1 shows the cases carried out.

Table 1 Experimental matrix

Case	Airfoil	AR	G	U_∞, m/s	V_{max}, m/s	T, s
1	NACA0012	4.86	1	0.17	0.17	1.35
2	NACA0012	4.86	2	0.17	0.34	1.35
3	NACA0012	4	1	0.26	0.26	0.59
4	NACA0012	4	2	0.26	0.52	0.59
5	Flat plate	4	1	0.26	0.26	0.59
6	Flat plate	4	2	0.26	0.52	0.59

The wing was towed with a trapezoidal speed profile with smoothed corners, accelerating over 4.5 chord lengths before reaching a constant tow speed. This towing velocity profile provided 60 chord lengths of travel at a constant speed before decelerating to rest. To ensure fully-developed flow, the wing traveled for 2.5 m or 21.7-32.8 chord lengths before plunging. A six-degree-of-freedom force balance (ATI Mini-40) provided data on forces. The measurement uncertainty of the force balance (95% confidence level) is 1.25% of full-scale load (40 N), which is equivalent to a 3.36% uncertainty in the peak lift for a $G = 2$ and $AR = 4.86$ plunge maneuver. To decrease the measurement uncertainty, each case in this study was repeated five times and ensemble averaged. A five run ensemble average is chosen based on the uncertainty

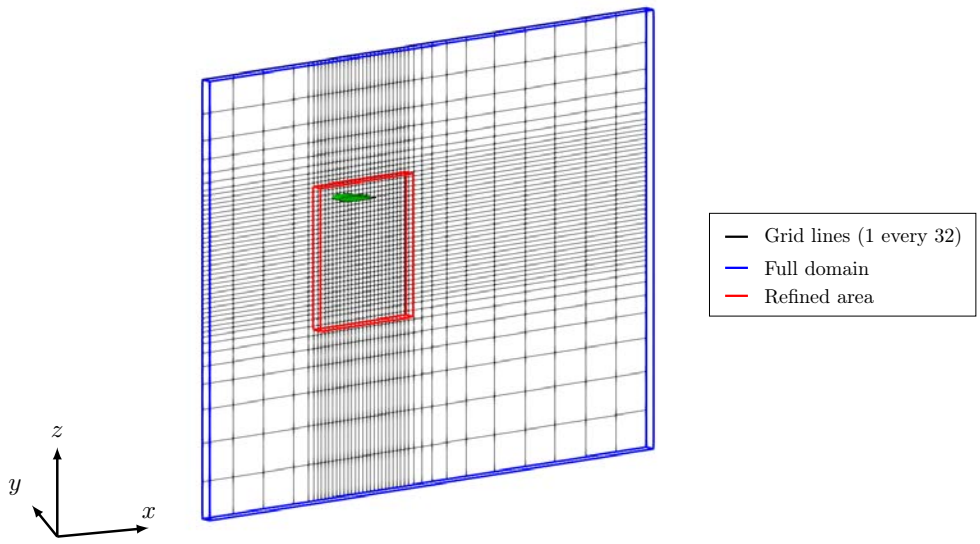

Fig. 2 Sketch of the computational domain.

analysis performed by Biler et al. [21]. Force data was sampled at 500 Hz, and the mean and standard deviation of each case across the five runs were found. To obtain the aerodynamic force contribution, the inertial force due to the acceleration of the wing and its mount during the plunging maneuver was obtained analytically and subtracted from the total measured force. The force coefficients presented in Sec. III were filtered using a zero-phase, digital Butterworth filter with a cut-off frequency of 5 Hz. Since the resulting force measurement uncertainty is relatively small, it is not shown in the force coefficients plots presented in this work.

C. Computational setup

The simulations have been performed with the in-house code TUCAN [22, 23], which solves the Navier-Stokes equations of the incompressible flow using a fractional step method on a non-uniform, Cartesian, staggered grid. The spatial discretization consists of second-order central differences for both convective and viscous terms. Time integration is performed with a low-storage, 3-stage, semi-implicit Runge-Kutta scheme. The wing is modeled using the immersed boundary method proposed by Uhlmann [24]. TUCAN has been extensively validated and employed for unsteady aerodynamics applications for infinite [25–27] and finite [28–30] aspect-ratio wings.

The simulations were performed by considering an infinite aspect-ratio wing, modelled by using periodic boundary conditions on a computational domain of finite span. The Reynolds number is fixed to $Re = 5000$, limited by computational resources. It was not possible to reach the values considered in the experiments. However, previous studies have shown that differences in the Reynolds number have a limited effect on the force coefficients even if they might have a considerable effect on the development and breakdown of vortical structures on the wing [31, 32].

A sketch of the computational domain is shown in Fig. 2. The computational domain size is $12c \times 0.25c \times 9.5c$ in streamwise, x, spanwise, y, and vertical, z, directions respectively. The inflow plane is located at $x/c = -3.5$. The top plane is located at $z/c = 3$. At $t = 0$, the leading edge of the wing is located at $x/c = 0$, $z/c = 0$, and at the end of the maneuver it is located at $z/c = -G$. The grid is uniform in the vicinity of the airfoil ($-0.5 < x/c < 2.5$, $-2.5 < z/c < 0.5$). The grid resolution in this region was defined after performing a grid refinement study in 2D simulations as reported by Moriche et al.[17], resulting in a grid spacing in all three directions of $\Delta x = c/320$. Far from the airfoil along the x and z directions the grid is stretched using a 1% stretching, except upstream where a 3% stretching is used. This results in a total number of grid points of $1335 \times 80 \times 1459$ along the x, y, and z directions, respectively.

As already mentioned, along the spanwise direction periodic boundary conditions are employed. At the inflow plane Dirichlet boundary conditions are imposed; at the outflow plane a convective boundary condition is imposed. At the top and bottom boundaries, free-slip boundary conditions are used. The initial condition for the maneuvers is determined by integrating the equations without moving the wing during a time interval in which the wake develops. A visualization of the flow field at the initial condition is shown in the Results section (see the top rows of Figures 5 and 6) . While for the NACA0012 wing the three-dimensionality of the flow is localized in a narrow region in the wake of the wing, for the flat plate three-dimensional structures can be seen already initially on top of the wing.

III. Results

A. Force coefficients

We start analyzing the time evolution of the lift coefficient, C_L, defined as

$$C_L(t) = \frac{L(t)}{\frac{1}{2}\rho U_\infty^2 S}, \tag{2}$$

where L is the lift, ρ is the density and S is the wing surface. In this work, we define the lift force as the vertical component (z) of the aerodynamic force to avoid having a lift with a time-dependent direction with large variations. This simplifies the analysis since, during the maneuver of case $G = 2$, the direction of the incoming flow velocity as seen in a coordinate system fixed to the wing has a variation of up to 60°. The curves of C_L for both experiments and simulations are shown in Figures 3a-b. Moriche et al. [17] divide the time evolution into three intervals. The first interval is the acceleration phase, $0 \leq tU_\infty/c \leq 1$, where the C_L grows rapidly until a peak is reached at an instant before the end of the interval. The force peaks earlier because the lift response is influenced by both plunge velocity and plunge acceleration, as discussed by Perrotta and Jones [15], and at the end of this interval the plunge acceleration is zero. During the acceleration phase, a strong LEV is developed and subsequently detaches from the wing. The second interval is the deceleration phase, $1 \leq tU_\infty/c \leq 2$, until the end of the maneuver. In this phase, the lift decreases

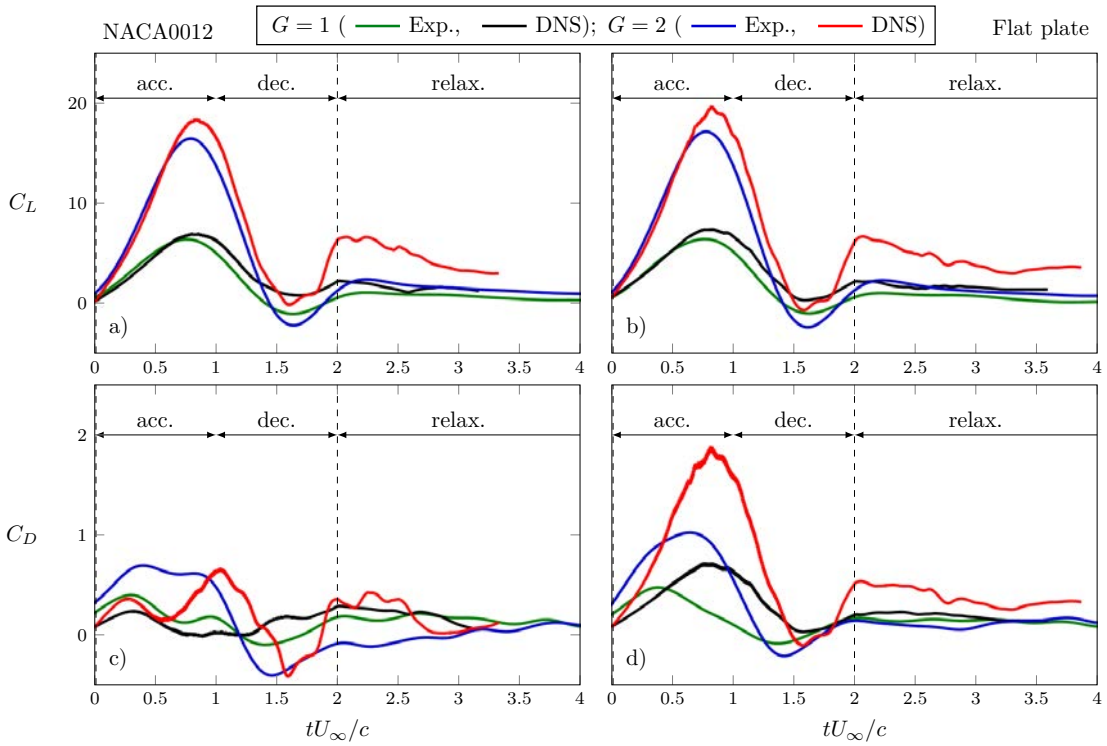

Fig. 3 Time history of lift (a, b) and drag (c, d) coefficients. $a), c)$ **NACA0012 wing.** $b), d)$ **Flat plate. Both wings,** $AR = 4$**.**

roughly until the middle of the interval where a local minimum is reached and then, while still decelerating at a reduced pace, the lift grows again. This trend coincides with the wing acceleration: at the mid of the interval the acceleration is minimum and then it grows until reaching a zero value at the end of the maneuver. Note also that during the final part of the interval the LEV that was left behind gets closer to the wing as the wing stops its motion, and therefore may have an influence on C_L. The third interval is the post-maneuver phase, where the lift coefficient slowly relaxes towards the corresponding static value.

Figures 3a and b show the time evolution of C_L including both experimental data for the wings with $AR = 4$ and DNS data. Overall, the curves obtained for the NACA0012 (figure 3a) present qualitative agreement, however there are some discrepancies that need to be highlighted. For both values of G, the growth of C_L during most of the acceleration phase is in good agreement between experimental and DNS data. The difference is that in the experiment $C_L^{\max}$ is reached earlier, and as a consequence is lower than the $C_L^{\max}$ in the DNS. In the deceleration phase, the decrease in C_L occurs roughly at the same rate in experiment and DNS, i.e. the curves are quasi-parallel. Also the difference between $C_L^{\max}$ and $C_L^{\min}$ is rather similar. However, since the $C_L^{\max}$ is lower in the experiment, then the $C_L^{\min}$ also reaches smaller values in the experiment compared to the DNS. The C_L recovery towards the end of the maneuver is qualitatively similar, however it seems more pronounced in the DNS, particularly for the case $G = 2$. The final phase of relaxation towards

the static values seems to be somewhat different in experiment and DNS. In the experiment, the C_L still grows a bit once the maneuver is finished (at $tU_\infty/c = 2$) reaching a local maximum at $tU_\infty/c \approx 2.2$. In the DNS, the growth of C_L seems to stop at the end of the maneuver. This is followed by a short plateau and then the decay towards the static value sets in. Note that since the value of C_L at the end of the maneuver is significantly higher in the DNS, the decay towards the static value needs to be more pronounced as well. This process does not seem to be monotonous, instead a few small oscillations are present. In the DNS the static value was not reached because the computation was stopped to save computational resources. In general, the same observations made for the NACA0012 can be made for the flat plate (figure 3b). A small difference in the DNS for the flat plate is that at the end of the maneuver, the C_L does not seem to present a short plateau.

Figures 3c and d show the evolution of the drag coefficient, C_D, defined as

$$C_D(t) = \frac{D(t)}{\frac{1}{2}\rho U_\infty^2 S}, \tag{3}$$

where D is the drag force, defined here as the horizontal component (x) of the aerodynamic force. Figure 3c shows the results for the NACA0012, where it can be seen that there is a good agreement between experiments and DNS for the case with $G = 1$ (note the differences in scale between lift and drag representations). For the higher velocity ratio $G = 2$, there is a visible discrepancy in the acceleration phase ($t/T < 1$), where the C_D predicted by the DNS is somewhat lower than in the experiments. During the deceleration phase ($1 < t/T < 2$) the evolution of C_D presents good agreement between experiments and DNS, however there is a small time shift between the two curves (analogous to the time shift observed in this phase for the C_L in figure 3a). The recovery towards the static value is preceded by an increase in C_D in the DNS, whereas in the experiment the static value is (almost) monotonically approached from the minimum of C_D reached in the deceleration phase. For the flat plate, while the trends are similar, more differences between experiments and simulations can be observed (figure 3d). First, the peak values of C_D for the flat plate are smaller by a factor of approximately 2 in the experiment compared to the DNS. Second, we observe that the time shift in the deceleration phase between experiments and DNS is a bit more pronounced in this case. Note that this time shift between experiment and DNS in the deceleration phase is observed for every combination of G and wing configuration presented in figure 3, except for the NACA0012 with $G = 1$.

There could be several reasons for the discrepancies discussed above. For example, in the experiments finite-wing effects might play a role via the interaction of wing-tip vortices with the LEV, leading to a different overall flow structure around the wing. This could include effects like those observed in finite-span dynamic stall, as discussed recently by Visbal and Garmann [33], as well as 3D effects in the wake [34]. The difference in the wing configuration could be responsible for the lower peaks of C_L observed in the experiments compared to the DNS (figures 3a and b). If this is the

case, it is not possible to reproduce such interactions in the DNS with an infinite aspect-ratio wing. Furthermore, the following aspects should be considered. First, the limited size of the computational domain along the wing span. This effect might have an influence on the development of flow structures in spanwise direction. It would be worthwhile to perform simulations with wider computational domains to test this hypothesis. Second, there exists the possibility that the discrepancies mentioned above could be a Reynolds number effect, since the experiments were performed at $Re = 20000$ and the DNS at $Re = 5000$. This difference in Reynolds number might affect the development of the boundary layers over the NACA0012 and the flat plate (and correspondingly, the development and detachment of the LEV [31, 32]). Also, a Reynolds number effect might be important in the stability and breakdown of the vortical structures generated during the maneuver, which will be analyzed in the following sections.

Another difference between experiments and simulations is the thickness of the flat plate. In the experiment, due to structural/manufacturing constraints, a thickness of 4.3% of the chord was employed. In the simulation the thickness of the flat plate can be estimated from the mesh width as 0.3% of the chord. This difference might have an impact in the discrepancies observed in the C_D of the flat plate between experiments and DNS (figure 3d). One possibility is that, in the experiments, the thicker section at the leading edge can withstand during some time the suction peak, similarly as in the case of the rounded leading edge of the NACA0012 wing. This is clearly less possible with the thinner section of the flat plate in the DNS. As a consequence, the drag obtained in the DNS is directly proportional to the lift, whereas in the experiment there might be some tilting of the total aerodynamic force towards the upstream direction, resulting in a small drag reduction.

The effect of airfoil shape and aspect ratio is explored using the experimental and numerical data in Fig. 4, that shows the time evolution of C_L and C_D obtained from every wing configuration for $G = 2$. The figure also includes an additional experiment in which the aspect ratio of the NACA0012 wing is $AR = 4.86$. The time history of C_L (figure 4a) suggests that the effect of airfoil shape is negligible in both experiments and DNS. However, small differences are observed near $C_L^{\max}$ and $C_L^{\min}$, with both higher $C_L^{\max}$ and lower $C_L^{\min}$ in the case of the DNS of the flat plate. Concerning the aspect ratio, the effect seems also to be negligible in the limited range covered in the study, $AR = 4$ and 4.86. The time evolution of C_D (Fig. 4b) tells a different story, with peak values during the maneuver four times larger for the flat plate than for the NACA0012 wing in the case of the DNS. We commented previously how the non-negligible thickness of the flat plate of the experimental configuration might result in a tilting of the force that is not present when an almost zero thickness flat plate is used, as in the DNS. Therefore, we focus the following discussion on the results obtained in the DNS. The shape of the curve in the case of the flat plate resembles the shape of the corresponding C_L curve. In fact, analyzing the peak values, they are consistent with an aerodynamic force which is perpendicular to the plate. If the latter

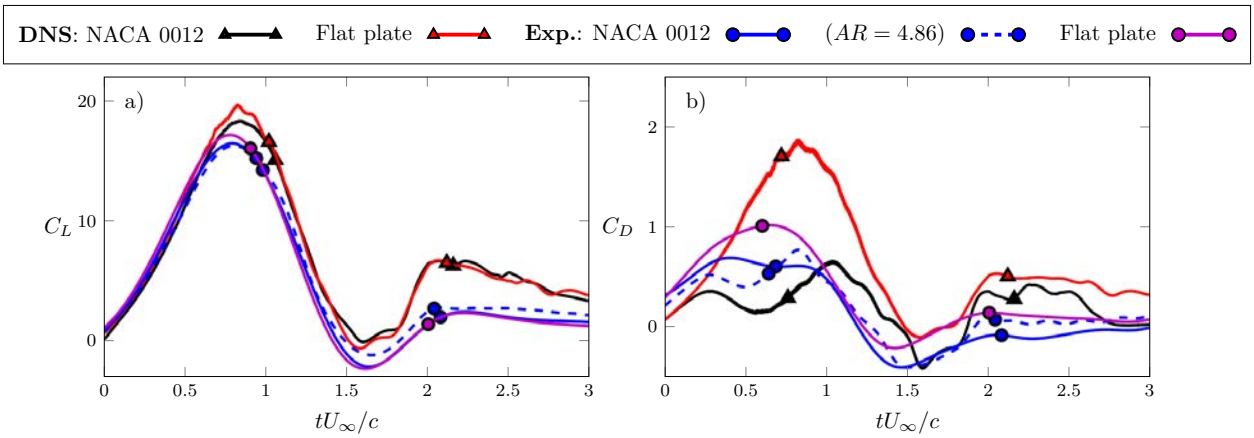

Fig. 4 Lift, a), and drag, b), coefficients as a function of time for case $G = 2$.

is defined by a normal force coefficient C_N, with a maximum value $C_N^{\max} = 20$ then

$$C_L^{\max} = C_N^{\max} \cos\alpha \approx C_N^{\max} = 20, \tag{4}$$

$$C_D^{\max} = C_N^{\max} \sin\alpha \approx C_N^{\max}\alpha = 1.745, \tag{5}$$

values which are consistent with the peak values obtained for the flat plate $C_L^{\max} = 19.66$ and $C_D^{\max} = 1.872$. The values for the NACA0012 wing are not consistent with this scenario, with $C_D^{\max} = 0.656$, and a C_D time evolution which does not resemble that of the corresponding C_L.

B. Flow visualization

We turn now our attention to the flow surrounding the airfoil during the maneuver using using flow visualizations of the DNS data. Figure 5 shows contours of spanwise vorticity averaged along the spanwise direction, $\overline{\omega}_y$. The flow structure for both flat plate and NACA0012 wing is qualitatively similar. First, during the initial acceleration phase LEV and TEV develop. At the end of this phase, $tU_\infty/c = 1$, the LEV and TEV are both already detached. The TEV will be subsequently convected downstream so that it does not have a significant influence on the lift coefficient. The contour of the LEV is more clearly defined in the case of the NACA0012, while for the flat plate the LEV seems more distorted. Below the LEV there is a dipole at the leading edge, from which the LEV in its rotation lifts vorticity up. During the deceleration phase the LEV grows in size and keeps lifting vorticity from the leading edge. At the end of the maneuver, $tU_\infty/c = 2$, the LEV is again in the vicinity of the wing, but closer to the TE. At this instant, the vorticity that has been lifted from the leading edge keeps the form of a dipole for the NACA0012 wing while for the flat plate the shape of this vorticity is blurred. Once the maneuver is over, $tU_\infty/c = 2.5$, the LEV is leaving the trailing edge, lifting vorticity from the rear part of the wing, forming a rather vertical shear layer of negative vorticity. In addition, a new LEV seems to be

forming for both cases; note that this new LEV will need to be released from the wing in order to reach at the end the same flow structure corresponding to the static case ($tU_\infty/c = 0$). This explains the long relaxation interval required to reach that condition.

Figure 6 gives information on the three-dimensionality of the flow, by displaying shaded contours of the standard deviation of the spanwise velocity component, u_y^{std}, with respect to the spanwise-averaged mean. This is shown on top of two contour lines of $\overline{\omega}_y$, that serve as reference for the position of the main vortical structures. Initially, for the NACA0012 wing the three-dimensionality of the flow is localized in the wake of the wing while for the flat plate three-dimensional structures are already present on top of the wing. As a consequence, the flow is highly 3D during the whole maneuver for the flat plate. For the NACA0012 instead, during the acceleration phase, 3D effects are only visible at the trailing edge. The TEV is surrounded by 3D structures. The LEV remains essentially 2D during the whole maneuver. At some instant, 3D effects travel quickly upstream via the boundary layer on top of the wing, an effect which is barely visible in Fig. 6, but that is clearly visible in corresponding animations. As a consequence, the LEV remains 2D but the vorticity that the LEV lifts from the airfoil is clearly three-dimensional. This effect is incipient at $tU_\infty/c = 1.5$ and clearly visible at $tU_\infty/c = 2$ and 2.5.

C. Force decomposition

The history of the force coefficients presented in the previous section shows that there are some differences between the experimental and numerical data, as well as between the flat plate and the NACA0012. In particular, it is unclear why the simulations yield higher C_L than experiments at the end of the maneuver ($tU_\infty/c \approx 2$). We also want to analyse why during the acceleration phase the drag coefficient of the flat plate is significantly higher than the drag coefficient of the NACA0012 wing. A quantitative analysis of force production is presented in this section.

In order to address these issues, we employ the force decomposition algorithm proposed by Chang [18, 19] and employed recently in various studies [26, 35]. An assessment of the advantages of this methodology compared to other methods (vortical impulse, wake integrals) has been also reported recently [36]. The main idea behind Chang's algorithm is that, if the hydrodynamic forces on a closed object immersed in an incompressible irrotational flow are zero (i.e., D'Alamberts paradox), then fluid elements with non-zero vorticity can be interpreted as sources of hydrodynamic force. Then, starting from the Navier-Stokes equations and making use of some projection functions (ϕ_x and ϕ_z), Chang

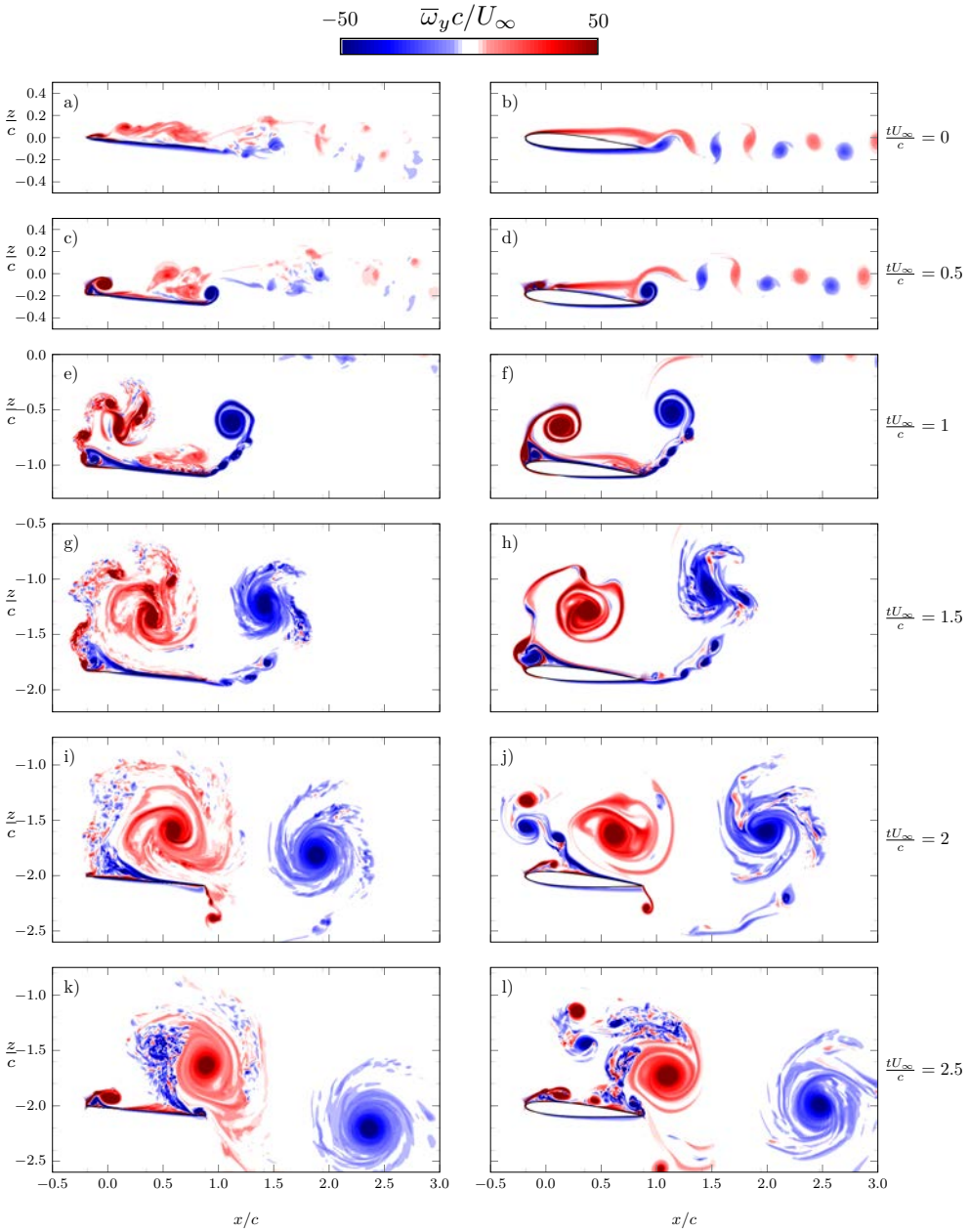

Fig. 5 Flow visualization of the DNS results with $G = 2$. Contours of $\overline{\omega}_y$. Left column, flat plate. Right column, NACA0012 wing.

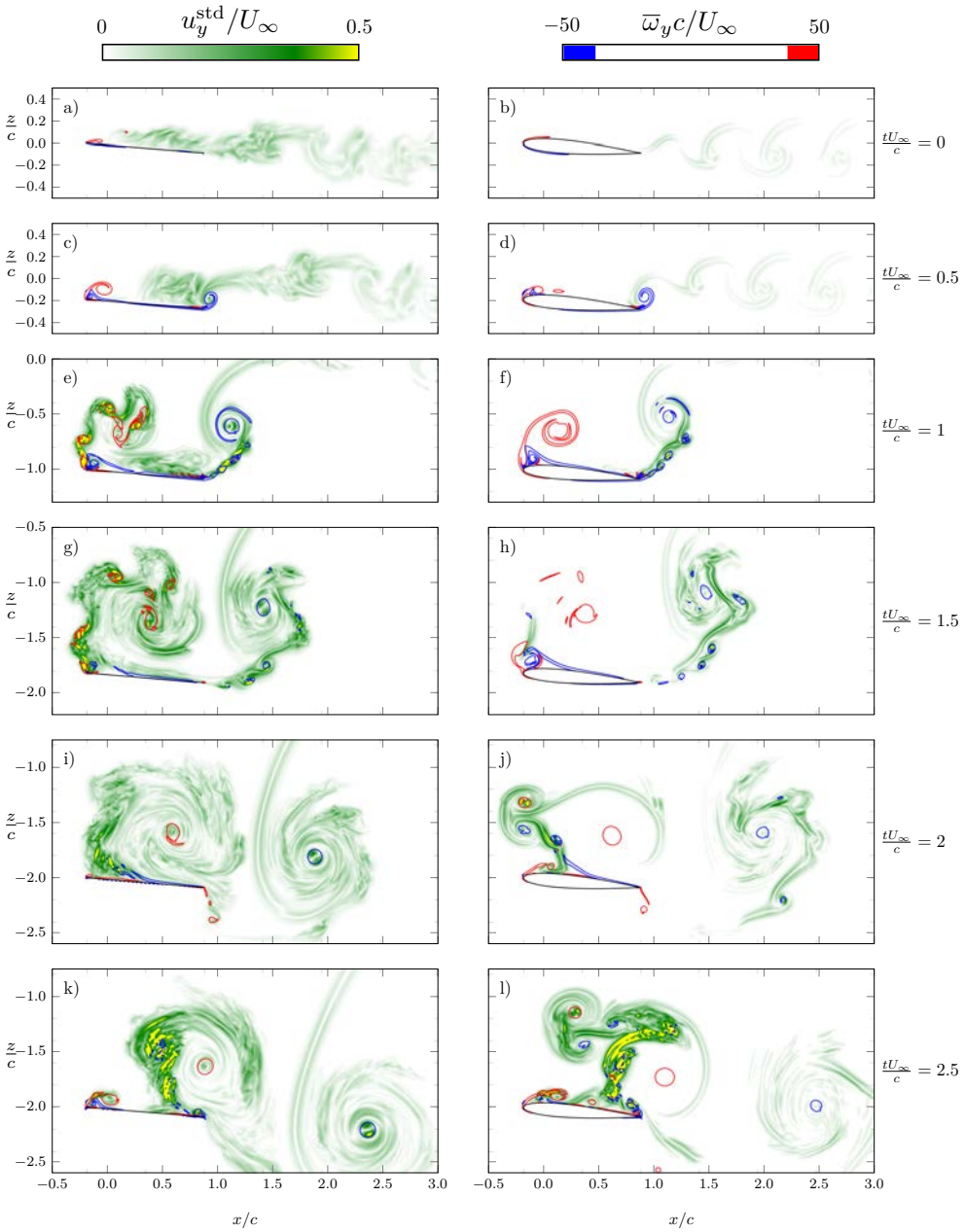

Fig. 6 Flow visualization of the DNS results with $G = 2$. Contour lines, $\overline{\omega}_y$. Shaded contours, u_y^{std}. Left column, flat plate. Right column, NACA0012 wing.

proceeds to decompose the aerodynamic forces as follows,

$$D = -\rho \int_S \frac{\phi_x}{U_\infty} \frac{\partial(\vec{u}+\vec{u}_w)}{\partial t} \cdot \vec{n}\, \mathrm{d}S + \frac{\rho}{2} \int_S |\vec{u}|^2 \vec{n} \cdot \vec{e}_x \, \mathrm{d}S - \rho \int_V (\vec{u} \times \vec{\omega}) \cdot \frac{\nabla \phi_x}{U_\infty} \, \mathrm{d}V + \mu \int_S (\vec{\omega} \times \vec{n}) \cdot \left(\frac{\nabla \phi_x}{U_\infty} + \vec{e}_x \right) \mathrm{d}S, \tag{6}$$

$$L = -\rho \int_S \frac{\phi_z}{U_\infty} \frac{\partial(\vec{u}+\vec{u}_w)}{\partial t} \cdot \vec{n}\, \mathrm{d}S + \frac{\rho}{2} \int_S |\vec{u}|^2 \vec{n} \cdot \vec{e}_z \, \mathrm{d}S - \rho \int_V (\vec{u} \times \vec{\omega}) \cdot \frac{\nabla \phi_z}{U_\infty} \, \mathrm{d}V + \mu \int_S (\vec{\omega} \times \vec{n}) \cdot \left(\frac{\nabla \phi_z}{U_\infty} + \vec{e}_z \right) \mathrm{d}S, \tag{7}$$

where $\vec{u}$ is the relative velocity of the fluid with respect to the wing, $\vec{u}_w$ is the wing velocity with respect to a reference frame which is at rest, $\vec{\omega}$ is the vorticity, μ is the dynamic viscosity, S represents the surface of the airfoil, V represents the fluid domain, $\vec{n}$ is the unit vector normal to the surface of the airfoil pointing towards the fluid, and $\vec{e}_x$ and $\vec{e}_z$ are the unit vectors in the x and z directions, respectively. The projection functions ϕ_x and ϕ_z are solutions to the Laplace equation, with suitable boundary conditions on the surface of the airfoil (more details in [18]).

In these expressions the first two terms of the right hand side can be grouped into the contribution to the force due to the motion of the body, the third term is the contribution of the vorticity within the flow and the fourth term is the contribution of the surface vorticity. The latter is usually small if the Reynolds number is not too low. As discussed in the literature [35, 36], in the absence of rotation of the wing, the contribution due to the motion of the body is exactly the same as the contribution from added mass from unsteady potential theory. One additional advantage of Chang's decomposition is that the integrand of the volume integral (third term of the right hand side) can be understood as a force density. Using Chang's words [18], the force density "*provides us a tool for examining how much an individual fluid element of non-zero vorticity contributes to the pressure force*".

We have applied the force decomposition algorithm to the DNS results for the case $G = 2$; the results for the case $G = 1$ are qualitatively similar and are omitted for brevity. We have integrated numerically all integrals in eq. (6-7) except those corresponding to the surface vorticity contributions, which have been obtained from the difference between the total force and the other two contributions. The projection functions have been obtained analytically for the case of the flat plate [35] and numerically for the case of the NACA0012 wing [26, 36]. In the following, we split the force coefficients in the three contributions using a superscript a for the added mass term, v for the vorticity within the flow and s for the surface vorticity.

$$C_L = C_L^a + C_L^v + C_L^s, \tag{8}$$

$$C_D = C_D^a + C_D^v + C_D^s. \tag{9}$$

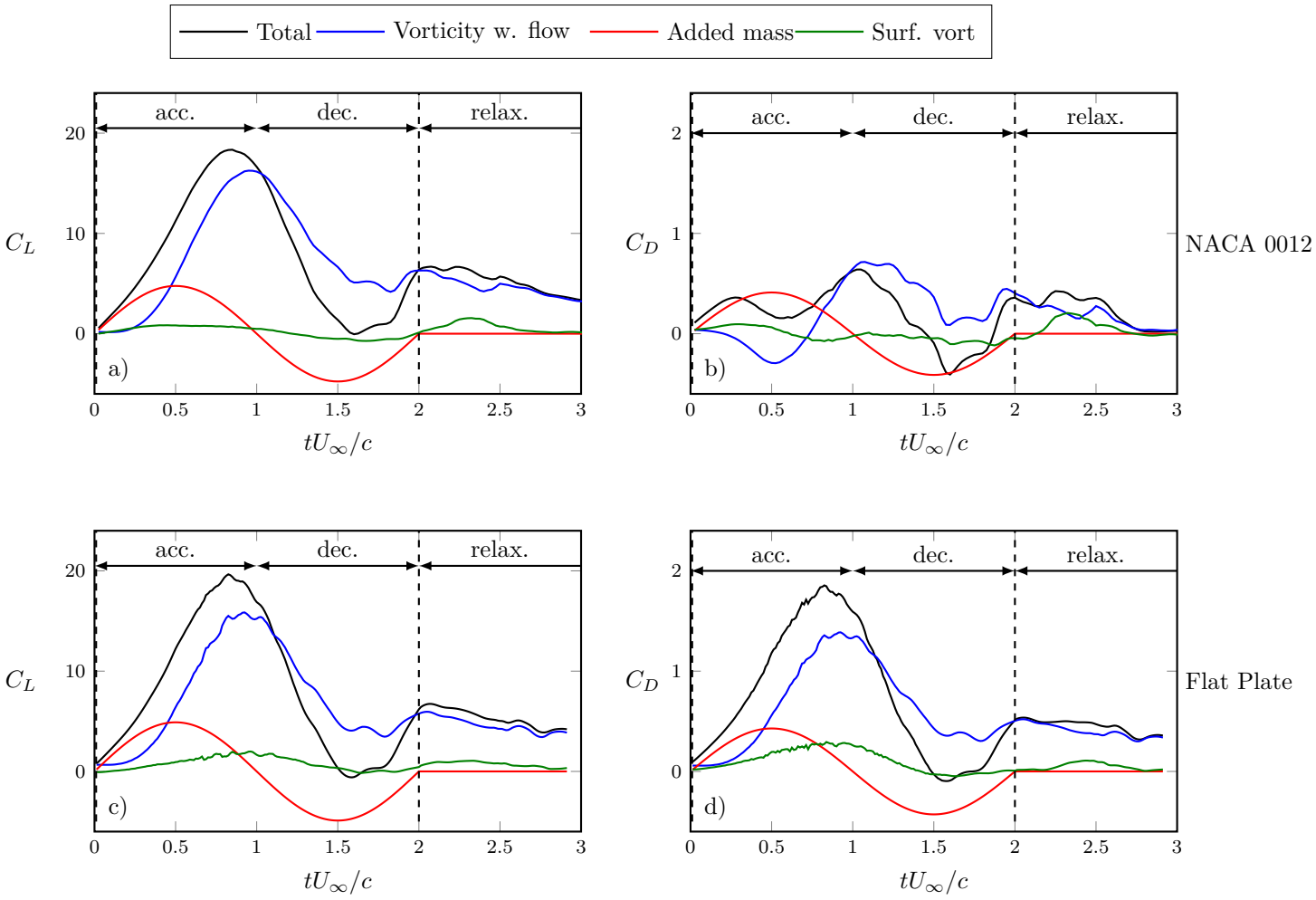

Fig. 7 Decomposition of the force coefficients for case $G = 2$. $a) - b)$ NACA0012 wing. $c) - d)$ Flat plate. $a), c)$ Lift. $b), d)$ Drag.

We also discuss below the force density of drag, δ_D, and the force density of lift, δ_L, which are the integrands of the volume integrals in eq. (6-7), correspondingly.

Figure 7 shows the decomposition of the force coefficients as a function of time for both wings, and Figure 8 shows the lift and drag densities at several time instants. Figure 7a and c show that, for both NACA0012 and flat plate, the time history of the three contributions to C_L are qualitatively similar. In both cases, the contribution from the vorticity within the flow is responsible for most of the positive peaks of C_L at $tU_\infty/c \approx 1$ and 2, while added mass effects seem to be responsible for the initial growth of C_L and the minimum at around $tU_\infty/c \approx 1.5$. For both cases, the contribution from the surface vorticity (viscous effects) is small.

Consistently with the discussion in section III.A, the contributions to C_D show significant dependence on airfoil shape, as observed by comparing figures 7b and d. For the NACA0012, the contribution from vorticity within the flow is initially negative. When the distributions of δ_L and δ_D at $tU_\infty/c = 0.5$ are analyzed (see figure 8f and h), we can see

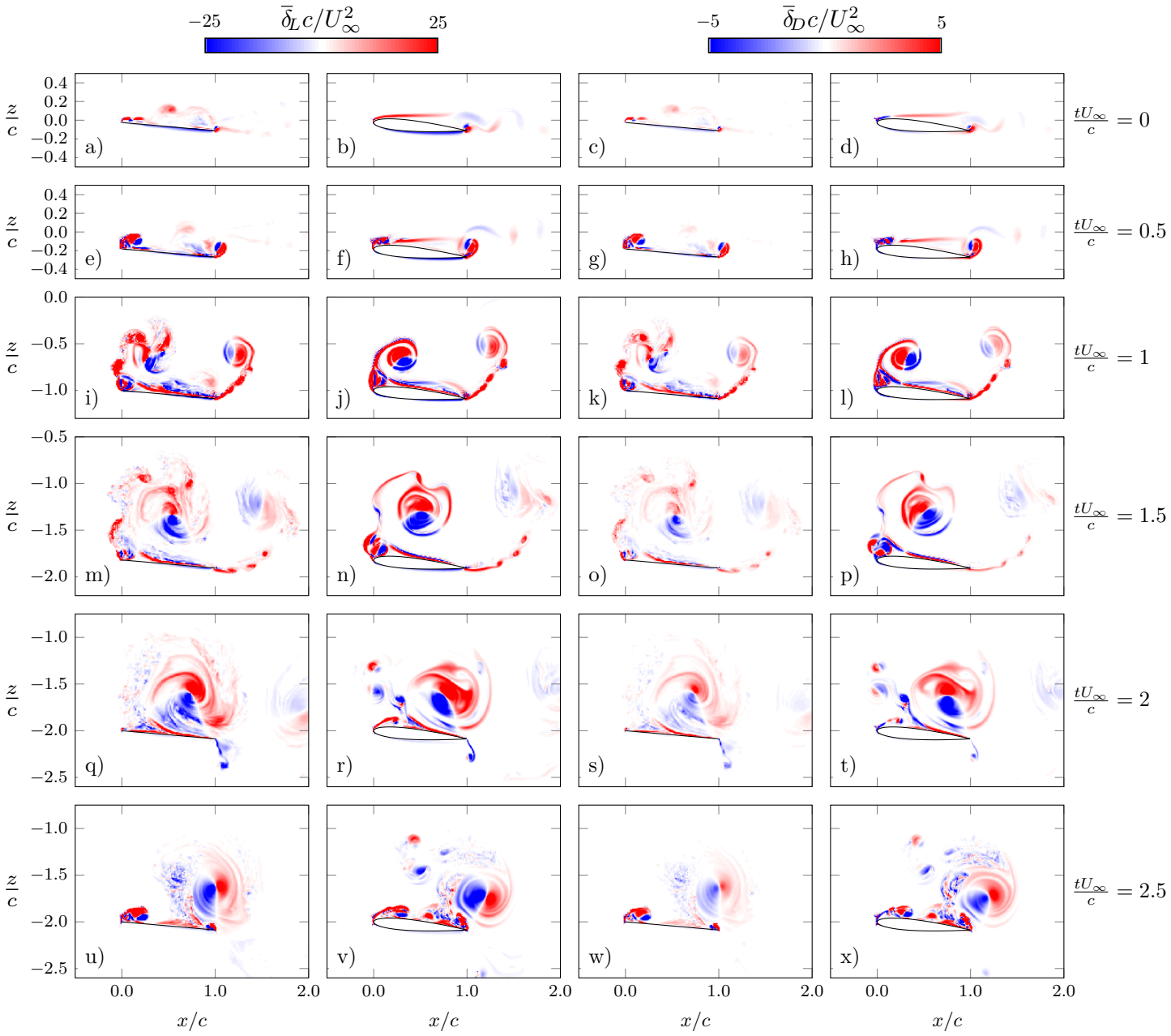

Fig. 8 Lift density (first two columns) and drag density (last two columns) at various time instants. First and third column, flat plate. Second and fourth column, NACA0012 wing.

that the vortical structures at the leading edge of the NACA0012 contribute positively to C_L and negatively to C_D, reflecting that the suction peak at the leading edge is producing lift and thrust. The situation for the flat plate is different: the suction peak forms on a flat surface facing up and downstream, resulting in lift and drag. Indeed, the contributions from the vorticity within the flow to C_L and C_D are proportional to each other (compare 7c and d), and so are the force densities δ_L and δ_D at every point in the computational domain (compare the first and third columns of figure 8).

Overall, figure 8 shows that the most prominent vortical structures of the flow (namely, the LEV and the TEV) contribute both positively and negatively to C_L^v and C_D^v, with their net contribution depending on the asymmetry between the positive and negative contributions. Note that this is an expected behaviour for δ_L and δ_D, due to their dependency on the Lamb vector, $\vec{u} \times \vec{\omega}$, as discussed by Chang [18] and Moriche et al. [26]. In order to quantify contributions to the vorticity within the flow component of the force, figure 9 shows the contribution to C_L^v and C_D^v from four different vortical structures: the leading edge vortex (LEV), the secondary vorticity (SV) generated below the LEV during the acceleration phase, the trailing edge vortex (TEV), and the secondary leading edge vortex (SLEV) developing upstream of the SV near the end of the maneuver. Note that LEV and SLEV have positive (clockwise) vorticity, while SV and TEV have negative (counterclockwise) vorticity. Using flow visualizations, we have identified these structures and defined non-overlapping regions of integration around them. Some of these structures are shown and labeled together with the corresponding integration regions in figure 9.

Overall, figure 9 shows that the major contributors to C_L^v and C_D^v during the maneuver are, in order of importance, first the LEV and then the TEV. Contributions from SLEV and SV are smaller, with the former becoming more important during the relaxation phase.

Figure 9c and d show that the results for the lift of the flat plate and the NACA0012 airfoil are qualitatively similar. The TEV contributes mainly during the acceleration phase, reaching a peak at the end of this phase. At $tU_\infty/c = 1$, the contribution of the TEV to C_L^v for the NACA0012 wing (flat plate) is 31% (34%) of the total. Beyond that time, the TEV is convected downstream and its contribution to the lift is negligible for $tU_\infty/c \gtrsim 1.5$.

The LEV contribution to lift behaves initially in a similar way as the TEV, growing during the acceleration phase, reaching its peak at $tU_\infty/c \approx 1$ and then starting to decline. At $tU_\infty/c = 1$, the contribution of the LEV to C_L^v for the NACA0012 wing (flat plate) is 58% (51%) of the total. However, as the maneuver progresses and the wing stops its motion the contribution of LEV to C_L^v grows again. In this time interval ($1.5 \lesssim tU_\infty/c \lesssim 2.25$) the LEV is clearly the major contributor to the lift. Thus, the results shown in figure 9 support the conjecture offered in the first paragraph of section III.A; namely that towards the end of the deceleration phase the LEV shed during the acceleration phase approaches the upper surface of the wing, producing a suction peak that yields a positive contribution to C_L^v. Interestingly, this could explain why the second maximum in C_L for $G = 2$ is not observed in the experiments: the LEV

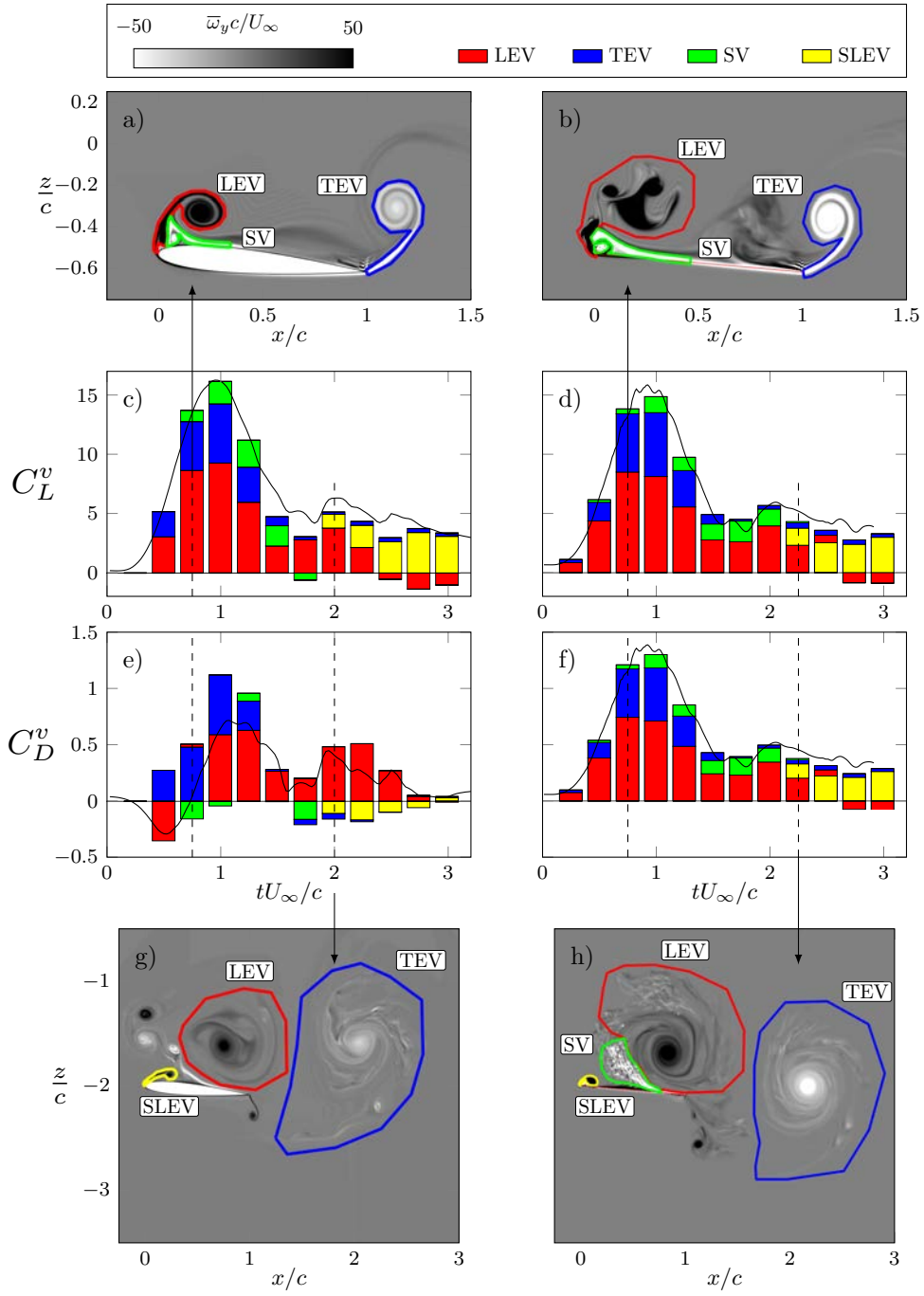

Fig. 9 *a), b), g), h)* **Flow visualization of case** $G = 2$ **at various instants indicating integration regions for each vortex structure.** *c) − f)* **Contributions to** C_L^v **and** C_D^v **of LEV, TEV, SV and SLEV as a function of time.** *a), c), e), g)* **NACA0012,** *b), d), f), h)* **flat plate.**

and TEV shed by finite aspect ratio wings dissipate much faster than those produced by airfoils or infinite aspect ratio wings due to the wake compression [34] and the vortex break-down caused by the non-linear interactions between LEV, TEV, and the wing tip vortices [37]. Also note that the Reynolds number is higher for the finite aspect ratio wings, which could also contribute to more unstable vortices and a quicker vortex break-down. Hence, one possible explanation is that the LEV in the experimental setup does not maintain its coherence for times long enough to approach the wing during the deceleration phase, resulting in higher values of C_L for DNS than for experiments at $tU_\infty/c \approx 2$. An alternative explanation with similar consequences for the lift coefficient is that, even if the LEV in the experimental setup mantains its coherence, the 3D interaction with TEV and tip vortices might result in a different trajectory of the LEV.

Figure 9c and d show that the contribution of SV to the lift is always relatively small, with contributions at the peak of about 10% for both wings. The SLEV is the major contributor to C_L^v during the relaxation phase (i.e., $tU_\infty/c \gtrsim 2.5$), as the LEV is advected downstream. Note also that during this later phase the effect of the LEV on the lift is negative.

Figures 9e and f show that the contributions to C_D^v from LEV, TEV, SLEV and SV are somewhat different for the NACA0012 and the flat plate. For the flat plate, the contributions from each structure to C_D^v are analogous to their contributions to C_L^v (compare figures 9d and f). This is in agreement with the conjecture offered in section III.A about the flat plate producing forces normal to the plate only. For the NACA0012, the LEV produces thrust (i.e., negative C_D^v) when it is attached and sufficiently close to the leading edge of the airfoil, consistent with the discussion of figure 8 in section III.B. The contribution of the LEV to C_D^v changes sign at about $tU_\infty/c = 0.75$ (i.e, just before C_L peaks), and the detached LEV remains as one of the major contributors to C_D^v throughout the rest of the maneuver. Analogous to the LEV, the SLEV produces thrust during the recovery phase, which explains the somewhat lower C_D observed for the NACA0012 than for the flat plate in figure 4b, both in experiments and simulations. The sign of the contribution of the SV to C_D^v seem to behave similarly to the signs of LEV (for $tU_\infty/c \lesssim 1.25$) and SLEV (for $tU_\infty/c \approx 1.75$), but shifted in time. This is probably to be expected, since the SV in the NACA0012 is produced relatively close to the leading edge (see figure 9a), contributing to the suction peak in a similar way as LEV and SLEV.

Finally, it is interesting to note that the C_D^v of the NACA0012 have non-negligible contributions from the boundary layer at the lower surface of the airfoil, not accounted by LEV, TEV, SLEV and SV. This contribution can be observed in figures 8 d,h and l, very close to the leading edge of the airfoil. Its contribution to C_D^v is negative (i.e., thrust), and seem to be specially important during the acceleration phase and the beginning of the deceleration phase, $tU_\infty/c \lesssim 1.25$, where figure 9e shows an imbalance between contributions of vortical structures (bars) and the total C_D^v (black line). Note that this imbalance is not observed for C_L^v in the NACA0012 and the flat plate, nor for C_D^v in the flat plate.

IV. Conclusions

We have presented experiments and direct numerical simulations of plunging maneuvers with velocity ratios $G = 1$ and 2, and with two different wings, a flat plate and a NACA0012 wing. The experiments were conducted at $Re = 20000$ with wings of two aspect-ratios that were towed in a water-filled towing-tank. The simulations were performed at $Re = 5000$ using a model of an infinite aspect-ratio wing by solving the Navier–Stokes equations using an immersed boundary method, prescribing the motion of the wing. We have analyzed the time evolution of the force coefficients during and after the maneuvers, supplemented with flow visualizations to characterize the development of vortical structures. We have also performed a force decomposition analysis to quantify the contributions of these vortical structures to the aerodynamic forces generated during the maneuver.

The plunge maneuver can be divided into three phases: acceleration, deceleration, and a post-maneuver phase in which the force coefficients evolve towards their steady state values. The comparison of the time history of C_L in experiments and simulations showed a good qualitative agreement during the acceleration and deceleration phases, with the DNS predicting a somewhat larger $C_L^{\max}$ during the acceleration and a somewhat smaller $C_L^{\min}$ during the deceleration phase. Moreover, the evolution of the lift coefficient during these two phases was qualitatively the same for NACA0012 airfoils and for flat plates, both for the spanwise-periodic wings of the DNS and for the finite aspect ratio wings (with aspect ratio $AR = 4$ and 4.86) used in the experiments. Interestingly, the drag coefficient of NACA0012 and flat plates differed considerably during the acceleration phase. This difference was ascribed to the orientation of the surface below the leading edge vortex (and the secondary vorticity developing beneath it). For the NACA0012, the curvature of the leading edge resulted in the associated suction peak producing lift and thrust. For the flat plate, an analogous suction peak resulted in lift and drag. This has been confirmed in the analysis of the contributions of different flow structures to the drag coefficient.

The largest discrepancies between experiments and simulations occurred in the aerodynamic response during the transition from the deceleration phase to the post-maneuver phase, where the DNS predicted significantly larger values of C_L than the experiments. Using the force decomposition algorithm proposed by Chang [18], we have observed that the major contributor to the force during this transition is the leading edge vortex shed during the acceleration phase, which approached the upper surface of the airfoil during its deceleration. Hence, we have conjectured that the observed difference between experiments and simulations might be related to the interaction of the leading edge vortex with the wing tip vortices. According to previous studies [34, 37], these interactions may cause a quicker dissipation of the leading edge vortex, or a change in its trajectory. Note that while wing tip vortices were present in the finite aspect ratio wings used in the experiments, they were not present in the spanwise-periodic wings used in the simulations. In addition, it should not be overlooked that differences in the Reynolds number between experiments and DNS could be responsible for some of the reported discrepancies. The literature shows [31, 32] that the Reynolds number has some

effect on the development and detachment of the LEV, and also on its stability and breakdown once it has been shed into the wake. These two effects might account for differences in the two maxima of the C_L curves, as shown in section III.C by the relatively large contribution of the LEV to C_L^v at these two instants.

Using the force decomposition analysis we have characterized the contributions to the lift and drag coefficient of the vortical structures occurring in the flow. The main leading edge vortex was found to be the major contributor during the whole maneuver while the trailing edge vortex was found to contribute mainly during the acceleration phase. In the post-maneuver phase as the main leading edge vortex was convected downstream, a secondary leading edge vortex was found to be the major contributor to the lift and drag during this final phase.

Acknowledgements

This work was partially supported by the State Research Agency of Spain (AEI) under grant DPI2016-76151-C2-2-R including funding from the European Regional Development Fund (ERDF), and the Air Force Office of Scientific Research under grant FA9550-16-1-0508. The computations were partially performed at the supercomputer Picasso from the *Red Española de Supercomputación* in activity FI-2019-1-0030.

References

[1] Martínez-Muriel, C., and Flores, O., "Analysis of vortical gust impact on an airfoil at low Reynolds number," J. Fluids Struct., in press, 2020.

[2] Mohamed, A., Massey, K., Watkins, S., and Clothier, R., "The attitude control of fixed-wing MAVS in turbulent environments," Prog. Aerospace Sci., Vol. 66, 2014, pp. 37 – 48.

[3] von Kármán, T., and Sears, W. R., "Airfoil theory for non-uniform motion," J Aeronautical Sci., Vol. 5, No. 10, 1938, pp. 379–390. doi:10.2514/8.674.

[4] Leung, J., Wong, J., Weymouth, G., and Rival, D., "Modeling transverse gusts using pitching, plunging and surging airfoil motions," AIAA J., Vol. 56, No. 8, 2018, pp. 3271–3278. doi:10.2514/1.J056961.

[5] Mulleners, K., Mancini, P., and Jones, A. R., "Flow Development on a Flat-Plate Wing Subjected to a Streamwise Acceleration," AIAA J., Vol. 55, No. 6, 2017, pp. 2118–2122. doi:10.2514/1.J055497.

[6] Granlund, K., Monnier, B., Ol, M., and Williams, D., "Airfoil longitudinal gust response in separated vs. attached flows," Physics of Fluids, Vol. 26, No. 2, 2014, p. 027103. doi:10.1063/1.4864338.

[7] Eldredge, J., Wang, C., and Ol, M. V., "A computational study of a canonical pitch-up, pitch-down wing maneuver," AIAA paper 2009-3687, 2009. doi:10.2514/6.2009-3687.

[8] Yilmaz, T. O., and Rockwell, D., "Flow structure on finite-span wings due to pitch-up motion," J. Fluid Mech., Vol. 691, 2012, pp. 518–545. doi:10.1017/jfm.2011.490.

[9] Jantzen, R. T., Taira, K., Granlund, K. O., and Ol, M. V., "Vortex dynamics around pitching plates," Phys. Fluids, Vol. 26, No. 5, 2014, p. 053606. doi:10.1063/1.4879035.

[10] Pitt Ford, C. W., and Babinsky, H., "Lift and the leading-edge vortex," J. Fluid Mech., Vol. 720, 2013, pp. 280–313. doi:10.1017/jfm.2013.28.

[11] Harbig, R. R., Sheridan, J., and Thompson, M. C., "Reynolds number and aspect ratio effects on the leading-edge vortex for rotating insect wing planforms," J. Fluid Mech., Vol. 717, 2013, pp. 166–192. doi:10.1017/jfm.2012.565.

[12] Garmann, D. J., and Visbal, M. R., "Dynamics of revolving wings for various aspect ratios," J. Fluid Mech., Vol. 748, 2014, pp. 932–956. doi:10.1017/jfm.2014.212.

[13] Sedky, G., Jones, A. R., and Lagor, F. D., "Lift Regulation During Transverse Gust Encounters Using a Modified Goman–Khrabrov Model," AIAA Journal, 2020, pp. 1–11. doi:10.2514/1.J059127.

[14] Wang, Z. J., "Vortex shedding and frequency selection in flapping flight," J. Fluid Mech., Vol. 410, 2000, pp. 323–341. doi:10.1017/S0022112099008071.

[15] Perrotta, G., and Jones, A. R., "Quasi-steady approximation of forces on flat plate due to large-amplitude plunging maneuvers," AIAA J., Vol. 56, No. 11, 2018, pp. 4232–4242. doi:10.2514/1.J057194.

[16] Perrotta, G., and Jones, A. R., "Unsteady forcing on a flat-plate wing in large transverse gusts," Exp. Fluids, Vol. 58, No. 8, 2017, p. 101. doi:10.1007/s00348-017-2385-z.

[17] Moriche, M., Gonzalo, A., Flores, O., and Garcia-Villalba, M., "Three-dimensional effects on plunging airfoils at low Reynolds numbers," AIAA J., 2020. doi:10.2514/1.J058569.

[18] Chang, C. C., "Potential flow and forces for incompressible viscous flow," Proc. R. Soc. A-Math. Phys. Sci., Vol. 437, No. 1901, 1992, pp. 517–525. doi:10.1098/rspa.1992.0077.

[19] Chang, C. C., Yang, S. H., and Chu, C. C., "A many-body force decomposition with applications to flow about bluff bodies," J. Fluid Mech., Vol. 600, 2008, p. 95–104. doi:10.1017/S0022112008000396.

[20] Hoblit, F. M., Gust loads on aircraft: concepts and applications, AIAA, 1988.

[21] Biler, H., Badrya, C., and Jones, A. R., "Experimental and Computational Investigation of Transverse Gust Encounters," AIAA Journal, Vol. 57, No. 11, 2019, pp. 4608–4622. doi:10.2514/1.J057646.

[22] Moriche, M., "A numerical study on the aerodynamic forces and the wake stability of flapping flight at low Reynolds number," Ph.D. thesis, Universidad Carlos III de Madrid, 2017. doi:10016/24960.

[23] Gonzalo, A., "Aerodynamic forces and vortex structures of flapping wings in forward flight," Ph.D. thesis, Universidad Carlos III de Madrid, 2018. doi:10016/28086.

[24] Uhlmann, M., "An immersed boundary method with direct forcing for the simulation of particulate flows," J. Comp. Phys., Vol. 209, No. 2, 2005, pp. 448–476. doi:10.1016/j.jcp.2005.03.017.

[25] Moriche, M., Flores, O., and Garcia-Villalba, M., "Three-dimensional instabilities in the wake of a flapping wing at low Reynolds number," Int. J. Heat and Fluid Flow, Vol. 62, 2016, pp. 44–55. doi:10.1016/j.ijheatfluidflow.2016.06.015.

[26] Moriche, M., Flores, O., and Garcia-Villalba, M., "On the aerodynamic forces on heaving and pitching airfoils at low Reynolds number," J. Fluid Mech., Vol. 828, 2017, pp. 395–423. doi:10.1017/jfm.2017.508.

[27] Moriche, M., Raiola, M., Discetti, S., Ianiro, A., Flores, O., and Garcia-Villalba, M., "Assessing aerodynamic force estimation with experiments and simulations of flapping-airfoil flows on the verge of three-dimensionality," Proc. Inst. Mech. Eng. G J. Aerospace Eng., 2019. doi:10.1177/0954410019867570.

[28] Gonzalo, A., Arranz, G., Moriche, M., Garcia-Villalba, M., and Flores, O., "From flapping to heaving: A numerical study of wings in forward flight," J. Fluids Struct., Vol. 83, 2018, pp. 293–309. doi:10.1016/j.jfluidstructs.2018.09.006.

[29] Arranz, G., Moriche, M., Uhlmann, M., Flores, O., and Garcia-Villalba, M., "Kinematics and dynamics of the auto-rotation of a model winged seed," Bioinspir. Biomim., Vol. 13, 2018, p. 036011. doi:10.1088/1748-3190/aab144.

[30] Arranz, G., Gonzalo, A., Uhlmann, M., Flores, O., and Garcia-Villalba, M., "A numerical study of the flow around a model winged seed in auto-rotation," Flow Turbul. Combust., Vol. 101, No. 2, 2018, pp. 477–497. doi:10.1007/s10494-018-9945-z.

[31] Visbal, M. R., "Numerical investigation of deep dynamic stall of a plunging airfoil," AIAA J., Vol. 49, No. 10, 2011, pp. 2152–2170.

[32] Jones, A. R., and Babinsky, H., "Reynolds number effects on leading edge vortex development on a waving wing," Exp. Fluids, Vol. 51, No. 1, 2011, pp. 197–210. doi:10.1007/s00348-010-1037-3.

[33] Visbal, M. R., and Garmann, D. J., "Dynamic stall of a finite-aspect-ratio wing," AIAA J., Vol. 57, No. 3, 2019, pp. 962–977. doi:10.2514/1.J057457.

[34] Green, M. A., Rowley, C. W., and Smits, A. J., "The unsteady three-dimensional wake produced by a trapezoidal pitching panel," J. Fluid Mech., Vol. 685, 2011, pp. 117–145. doi:10.1017/jfm.2011.286.

[35] Martín-Alcántara, A., Fernández-Feria, R., and Sanmiguel-Rojas, E., "Vortex flow structures and interactions for the optimum thrust efficiency of a heaving airfoil at different mean angles of attack," Phys. Fluids, Vol. 27, No. 7, 2015, p. 073602. doi:10.1063/1.4926622.

[36] Martín-Alcántara, A., and Fernández-Feria, R., "Assessment of two vortex formulations for computing forces of a flapping foil at high Reynolds numbers," Phys. Rev. Fluids, Vol. 4, No. 2, 2019, p. 024702. doi:10.1103/PhysRevFluids.4.024702.

[37] Arranz, G., Flores, O., and Garcia-Villalba, M., "Three-dimensional effects on the aerodynamic performance of flapping wings in tandem configuration," J. Fluids Struct., Vol. 94, 2020, p. 102893. doi:10.1016/j.jfluidstructs.2020.102893.